Published at Colloids and Surfaces B : Biointerfaces 185 (2020) 110612

Differential properties and effects of fluorescent carbon nanoparticles towards intestinal theranostics

L. Vallan,[1] J. Hernández-Ferrer,[1] L. Grasa,[2,3,4] J.M. González-Domínguez,[1] M.T. Martínez,[1] B. Ballesteros,[5] E.P. Urriolabeitia,[6], A. Ansón-Casaos,[1,*] A.M. Benito,[1] W.K. Maser[1]

[1]Instituto de Carboquímica, ICB-CSIC, Miguel Luesma Castán 4, 50018 Zaragoza, Spain

[2]Departamento de Farmacología y Fisiología, Facultad de Veterinaria, Universidad de Zaragoza, Miguel Servet, 177, Zaragoza, 50013, Spain

[3]Instituto de Investigación Sanitaria de Aragón (IIS), Zaragoza, Spain

[4]Instituto Agroalimentario de Aragón – IA2 –, (Universidad de Zaragoza – CITA), Zaragoza, Spain

[5]Catalan Institute of Nanoscience and Nanotechnology (ICN2), CSIC and the Barcelona Institute of Science and Technology, Campus UAB, Bellaterra, Barcelona, 08193, Spain

[6]Instituto de Síntesis Química y Catálisis Homogénea, ISQCH, CSIC, Universidad de Zaragoza, Pedro Cerbuna 12, Zaragoza, 50009, Spain

[*]Corresponding author E-mail: alanson@icb.csic.es

Abstract

Given the potential applications of fluorescent carbon nanoparticles in biomedicine, the relationship between their chemical structure, optical properties and biocompatibility has to be investigated in detail. In this work, different types of fluorescent carbon nanoparticles are synthesized by acid treatment, sonochemical treatment, electrochemical cleavage and polycondensation. The particle size ranges from 1 to 6 nm, depending on the synthesis method. Nanoparticles that were prepared by acid or sonochemical treatments from graphite keep a crystalline core and can be classified as graphene quantum dots. The electrochemically produced nanoparticles do not clearly show the graphene core, but it is made of heterogeneous aromatic structures with limited size. The polycondensation nanoparticles do not have C=C double bonds. The type of functional groups on the carbon backbone and the optical properties, both absorbance and photoluminescence, strongly depend on the nanoparticle origin. The selected types of nanoparticles are compatible with human intestinal cells, while three of them also show activity against colon cancer cells. The widely different properties of the nanoparticle types need to be considered for their use as diagnosis markers and therapeutic vehicles, specifically in the digestive system.

Keywords: carbon dot; graphene quantum dot; polymer dot; fluorescence; biocompatibility; toxicity

1. Introduction

Fluorescent carbon nanoparticles were mentioned for the first time in 2004, by the group of W. A. Scrivens upon investigating an electrophoretic method for the purification of single-walled carbon nanotubes produced by arc-discharge [1]. This process revealed the presence of a fluorescent fraction, which was later characterized and found to consist of carbonaceous

fluorescent nano-sized material. From that moment on, the interest of the scientific community for carbon nanoparticles grew incessantly, as the surprising fluorescence properties, together with the astounding applicative potential, were rapidly disclosed. At the state of the art, fluorescent carbon nanoparticles are a well-known subject of study in many fields, thanks to the excellent performance demonstrated in photovoltaic applications, sensing, bioimaging and drug delivery [2]. In particular, hybrid biomedical probes based on carbon nanoparticles show improved water solubility, photo-stability, targeting properties, sensitivity and biocompatibility [3-7].

Among fluorescent carbon nanoparticles, an important subclass is represented by graphene quantum dots (GQDs), whose distinctive trait lies in the extended π-conjugation of their structure, consisting of one or few layers of graphene oxide (GO) with lateral size inferior to 10 nm [8]. The preparation of GQDs is commonly a top-down process involving the oxidative cutting of bigger conjugated carbon structures, such as graphite [9], GO [10], coal [11] or carbon nanotubes [12]. A wide number of harsh treatments can serve this purpose, including the employment of strong acids and oxidants, high temperatures, electrochemical oxidation, microwave irradiation or sonication [13]. It has been shown that the acid cleavage on carbon materials preferentially attacks to zig-zag edges, generating an oxidation fringe that divides the graphene sheet into smaller pieces [14]. In the electrochemical method, the oxidation mechanism is mediated by the highly reactive non-selective hydroxyl radical [15, 16].

The choice of the preparation protocol is critical for determining the final properties of GQDs. In particular, the optical behavior strictly depends on the size and chemical functionalization of the conjugated π-domains [17], which determine the energy of the delocalized states responsible for the fluorescence emission. Even the GQD suitability for specific applications is driven by the choice of the preparation method. For example, the employment of GQDs for biomedical applications *in vivo* requires their complete water solubility and biocompatibility, which is

depending on the size and the oxidation state of the nanoparticles [18]. Besides, oxygenated functional groups supply excellent reactive sites for the preparation of drug nanocarriers [19]. Besides, the preservation of the sp^2 conjugation might be essential for the implementation of the GQDs in optoelectronic devices, such as light emitting diodes [20] or photovoltaic cells [21]. In such cases, the synthesis of nanoparticles should not affect the integrity of the π-domains and thus the cleavage should be mild.

Depending on the application to consider, other fluorescent carbon nanoparticles, generally called carbon dots (CDs), offer an interesting alternative to GQDs. CDs are frequently prepared by bottom-up procedures, including the hydrothermal treatment, microwave irradiation or pyrolysis of small organic molecules or polymers. The as-formed nanoparticles normally show highly amorphous polymeric structures, which can include (or not) conjugated π-domains or molecular fluorophores [22-24]. High water solubility, an abundance of organic functional groups and environment-sensitive fluorescence are properties that make CDs another promising class of carbon particles, complementary to GQDs, for the preparation of bio-related nanomaterials [25].

Given the huge number of strategies for the preparation of fluorescent carbon nanoparticles, resulting in an extreme variability of their chemical and optical properties, opportune comparisons between different methodologies are certainly helpful for the correct understanding of these nanostructures and for the weighted choice of the protocol in view of specific applications. In particular, the surface chemistry and luminescence properties are key issues for the use of carbon nanoparticles in biomedicine as imaging and photodynamic therapy platforms [26]. It has been reported that GQDs under visible light generate singlet oxygen that might affect cancer cells [27]. A wide absorption range in the visible-near infrared region, together with fluorescence, makes the carbon nanoparticle a combined imaging and therapeutic agent [27].

In this work, four different procedures for the preparation of fluorescent carbon nanoparticles are explored, including three types of GQDs and one type of CDs. The size, structure and optical properties of the materials are studied and compared, to identify similarities and differences between the employed methodologies. In particular, the preservation of π-domains and the amount and type of oxygen moieties are discussed, as well as their influence on the fluorescence emission. A sequential classification of synthesis methods is deduced, according to the number and size of π-domains. Besides, it is directly evidenced that fluorescence in carbon nanoparticles originates from different radiative mechanisms, even when the nanoparticles are typically called with the generic name of GQDs. Finally, the cytotoxicity of nanoparticles on cells of the human intestine epithelium is studied, in view of bioimaging and drug delivery applications. The nanoparticle effect is assessed at two levels of cell differentiation, which respectively represent cancer and normal cells.

2. Experimental

Graphene-like carbon materials are excellent precursors for the preparation of GQDs. In this work, three distinct routes starting from graphite precursors were explored. The first type of GQDs was obtained by wet chemistry (W-GQD) according to a modified Hummers method, where sulphuric acid, sodium nitrate and potassium permanganate at high temperatures and long reaction times produced the complete cleavage of graphite into small, oxidized nanoparticles. In another route, prolonged sonication promoted the cleavage of GO through the production of thousands of bubbles, whose formation and collapse generate extremely high pressures on the GO sheets, helping the oxidative cutting performed by the NO_2 gas generated upon mixing sulphuric and nitric acid. In this way, the sonochemistry-based GQDs (S-GQDs) were obtained. Finally, another material was prepared through the electrochemical oxidation of a graphite anode and is labelled as E-GQD. Here, water is oxidized under a high potential to

generate oxygen and hydroxyl radicals, which trigger the exfoliation and oxidation of the anode. The properties of electrochemically synthesized GQDs depend strongly on the strategy of preparation and the experimental conditions [6, 28-30]. Here, the production of E-GQDs was achieved using a new, scalable "switching two-electrode" galvanostatic method using cheap and non-toxic materials. Besides these approaches, which all entail the fragmentation of bigger carbon materials, the fourth class of nanoparticles was obtained starting instead from molecular precursors. Citric acid and ethylenediamine were employed for the microwave-mediated formation of nano-sized amorphous particles, simply labelled as carbon dots (CDs).

2.1. Synthesis methods

2.1.1. Preparation of W-GQDs

Graphite powder (1.0 g, Sigma-Aldrich) was put into a 250 ml round bottom flask. Next, 100 ml of sulfuric acid and 43 g of sodium nitrate were slowly added while stirring. Afterwards, the flask was cooled in an ice-bath and 3.0 g of potassium permanganate was added little by little, in order to keep the temperature below 5°C. After that, the potassium permanganate was completely dissolved, the temperature was raised up to 160°C and the dispersion was left for 2 hours under stirring. Afterwards, the dispersion was dialyzed in ultrapure water (MWCO: 2 kDa, 5 days). The final water solution was heated in an autoclave at 160°C for 24 hours, filtered through a 0.1 µm pore size filter and freeze-dried to recuperate the solid product W-GQDs.

2.1.2. Preparation of S-GQDs

Six sealed glass vials containing 10 mg of GO and 2.5 mL of an acidic mixture (concentrated H_2SO_4/HNO_3 mixture, 3:1) were sonicated for 24 h at 80°C using an ultrasound bath, under intermittent periods of 8 h, with an overnight settlement between them. Afterwards, vials were allowed to cool down to room temperature and the dark brown liquids contained in each vial were carefully diluted with deionized water up to 20 mL and hand-shaken for a few seconds.

After settling down at room temperature overnight, hand-shaking was again performed and the orange solutions were gathered together and transferred into dialysis sacks (Spectrum Labs, SpectraPor® MWCO 6-8 kDa). The dialysis against deionized water took place in a 5 L beaker, with frequent water replacements, until the pH of the outer waters became neutral. The dialysis system was protected from light with aluminum foil. It is important to mention that a careful and thorough tracing of the dialysis process was undertaken, and no fluorescence was ever noticed in the dialysis waters, neither carbonaceous solids upon filtrating them, meaning that GQDs fully remained inside the dialysis sacks. Once neutralized, the resulting yellow solution of GQDs was taken out from the sacks, protected from the light and stored at 3-4°C until further characterization or use. By freeze-drying, a spongy and low density solid was obtained.

2.1.3. Preparation of E-GQDs

The electrochemical synthesis was carried out using an Autolab PGSTAT302N potentiostat/galvanostat. 25 ml of a 0.1 M phosphate buffer solution, pH 6.86, was employed as the supporting electrolyte. Mono- and disodic sodium phosphate were purchased from Sigma-Aldrich. Two identical graphite rods (CYMIT Química, Spain) were used as working electrodes. Galvanostatic cycle synthesis was carried out using a current of ± 0.35 A, switching the behavior of the graphite rods as anode or cathode every 10 s, completing 800 cycles. This two-electrode configuration in a small cell allowed obtaining higher concentrations in a reproducible scalable process. The resulting suspensions were filtered through a 0.2 µm pore size filter and further separated by centrifugation at 5500 rpm for 30 minutes using 9 kDa molecular weight cut-off membranes. The filtered solution was dialyzed (MWCO: 2 kDa, 5 days) to remove the supporting electrolyte, and then freeze-dried, obtaining E-GQDs in the form of grey powder.

2.1.4. Preparation of CDs

Citric acid monohydrate (2.0 g, 9.5 mmol) was dissolved in ultrapure water (16 mL). Upon addition of ethylenediamine (0.64 mL, 9.5 mmol), the solution was heated through microwave irradiation. The microwave-assisted reaction was performed in a CEM Discover SP reactor working in the open-batch modality. The mixture was irradiated in order to keep the temperature at 140°C for 6 min and then irradiation was stopped. This yielded a yellow, transparent, solid product, highly soluble in water. The product was dissolved in ultrapure water and dialyzed against ultrapure water (MWCO=0.5–1.0 KDa, 3 days, twice a day). Dry CDs were obtained by freeze-drying.

2.2. Characterization techniques

High resolution transmission electron microscopy (HRTEM) images were acquired on a FEI Tecnai G2 F20 operated at 200 kV. The samples were deposited onto a copper grid coated with an ultrathin carbon on holey carbon film from a dispersed solution in water.

Atomic force microscopy (AFM) images were acquired in air under ambient conditions using either NT-MDT or Veeco instruments in the tapping mode. The NT-MDT Aura NTEGRA was operated at 110 kHz resonance with Au tips HA_NC ETALON (10nm curvature radius). Samples were prepared on silica substrates by drop casting of dilute water solutions. The Veeco Multimode SPM was provided with the Nanoscope V controller, J-scanner and the Nanoscope Analysis version 1.5 software. Veeco cantilevers of antimonium (n)-doped Si RTESPA PART MPP-11120 were used, with a resonance frequency in the range of 247-306 Hz and a force constant of 20-80 $N \cdot m^{-1}$. A drop of the nanoparticle dispersion was deposited on mica substrates and left to dry.

Infrared (IR) absorption measurements were performed on powder samples pressed with KBr into pellets with a Bruker Vertex 70 spectrometer. ^{1}H and ^{13}C nuclear magnetic resonance (NMR) spectra were recorded in D_2O solutions at 25ºC on a Bruker AV500 spectrometer (δ in

ppm and J in Hz) at a ^{1}H NMR operating frequency of 500.13 MHz. ^{1}H and ^{13}C NMR spectra were referenced using the solvent signal as an internal standard. X-ray photoelectron spectroscopy (XPS) measurements were taken with an ESCAPlus spectrometer using either Mg or Al anode. XPS data analysis was performed with casaXPS software. UV/Vis absorption spectra were recorded on a Shimadzu UV-2401 PC spectrophotometer. Photoluminescence excitation and emission spectra were recorded on a Horiba Jobin Yvon Fluoromax-P. All the spectra were recorded at room temperature using a 10 mm path-length quartz cuvette.

2.3. Cell culture and viability assay

This study was carried out in the human enterocyte-like cell line Caco-2/TC7 [31], kindly provided by Dr. José Emilio Mesonero (Universidad de Zaragoza, Zaragoza, Spain). This cell line undergoes in culture a process of spontaneous differentiation that leads to the formation of a monolayer of cells, expressing morphological and functional characteristics of the mature enterocytes. This differentiation process is growth-dependent, where the cells undergo differentiation from 'undifferentiated proliferative crypt-type cells' in the exponential phase of growth, to 'differentiated enterocyte-type cells' in the stationary phase [32]. Caco-2/TC7 cells (passages 30-50) were cultured at 37ºC in an atmosphere of 5% CO_2 and maintained in high glucose DMEM supplemented with 2 mM glutamine, 100 $U \cdot mL^{-1}$ penicillin, 100 $\mu g \cdot mL^{-1}$ streptomycin, 1% non-essential amino acids, and 20% heat-inactivated fetal bovine serum (FBS) (Life Technologies). To cell line maintenance, cells were passaged enzymatically with 0.25% trypsin-1 mM EDTA and sub-cultured on 25 cm^2 plastic flasks at a density of 10^4 $cells \cdot cm^{-2}$. Culture medium was replaced every 2 days. With this density of culture, the cells reach cell confluence 90 % (where cell differentiation starts) at 7 days after seeding, and the complete cell differentiation is reached at 15 days post-seeding. Thus, experiments in undifferentiated and differentiated cells (considered as cancer and normal cells, respectively)

were performed between 1-4 days and 11-14 days post-seeding, respectively. Cells were seeded in 96-well plates at a density of 2×10^4 or 4×10^3 cells per well, and measurements were carried out 4 or 14 days after seeding, respectively. The culture medium was replaced with fresh medium (without FBS) containing the samples at the required concentrations and with an exposure time of 72 h.

Cell survival was measured using the MTT test. The assay is dependent on the cellular reduction of 3-(4,5-dimethylthiazol-2-yl)-2,5-diphenyltetrazolium bromide (MTT, Sigma) by the mitochondrial dehydrogenase of viable cells to a blue formazan product that can be measured spectrophotometrically. Following the appropriate incubation of cells, with or without the samples, MTT (5 mg mL^{-1}) was added to each well in an amount equal to 10 % of the culture volume. Cells were incubated with MTT at 37 °C for 3 h. After that, the medium and MTT were removed and 100 µl of DMSO was added to each well. The plate was gently stirred in a shaker. Finally, the cell viability was determined by measuring the absorbance with a multi-well spectrophotometer (DTX 800 Multimode Detector, Beckman Coulter) at a wavelength of 560 nm and compared with the values of control cells incubated in the absence of the samples. Experiments were conducted in triplicate wells and repeated at least four times.

3. Results and discussion

3.1. Structure

The size characterization of the samples was performed by high-resolution TEM (Figure 1) and AFM (Figure 2) analysis. TEM images show W-GQDs and S-GQDs nanoparticles with similar lateral size, ranging between 3 and 6 nm for both. Moreover, crystalline planes spaced by 0.21 nm are observed inside the nanoparticles, evidencing the presence of a graphene structure. AFM analysis of W-GQD nanoparticles reveals a thickness in the range of 0.8 to 2.3 nm. Therefore,

considering GO sheets as separated by approximately 0.7 nm, W-GQD nanoparticles are formed by one to three graphene layers. The TEM analysis of E-GQDs shows a high rate of aggregation, hindering particle size measurement. AFM images also showed aggregation, but more individual E-GQDs were observed, suggesting that the difficulty for their observation by TEM can be related to a strongly altered graphene structure. The analysis of the height profile by AFM shows an average size of 1.5 ± 0.15 nm for individual E-GQDs, although larger aggregates are also observed. Finally, the AFM characterization of CDs showed that the sample consists of nanoparticles comprised between 1 and 2 nm, in good agreement with TEM results showing a particle size around 2 nm.

Once proved that all the synthesis methods effectively produced nanoparticles, the composition of the samples was characterized by means of IR analysis and XPS. A comparison between the chemical structures of each sample allowed a better understanding of their chemical nature and of the mechanisms involved in the different synthetic methods.

Relevant information about the chemical structure of the carbon core can be deduced from IR spectra (Figure 3, Table 1). In W-GQDs, S-GQDs and E-GQDs, the sp^2 conjugation of the graphite precursor materials is not entirely lost after the cleavage process, as it is demonstrated by their respective absorption bands at 1610, 1626 and 1643 cm^{-1}, corresponding to the C=C stretching. However, their different positions apparently indicate an evolution in graphene domains, which become smaller and more heterogeneous in the order of W-GQDs > S-GQDs > E-GQDs. In fact, the E-GQD sample shows a vinyl band at 943 cm^{-1} and methylene bands at 2860/2932 cm^{-1} that can be associated with the transformation of graphite aromatic structures into aliphatic and alkyl chains. The CD sample does not present C=C bonds, and instead shows a prominent wide band of methylene groups at 2928/3079 cm^{-1}.

The IR analysis was helpful for the identification of oxygenated functional groups. Moreover, the extensive presence of oxygen moieties in the samples sheds light on the oxidation pathways

promoting the formation of the nanoparticles. As shown in Figure 3 and Table 1, all the samples show a clear band between 1709 and 1780 cm^{-1} due to the C=O stretching of carboxylic acid, free or involved in hydrogen bonds. Additionally, the band at 1815 cm^{-1} (S-GQDs) denotes the presence of cyclic acid anhydrides, which can form through the acid-catalyzed condensation of adjacent carboxylic acids.

In the four nanoparticle samples, absorption bands in the range of 1120-1235 cm^{-1} can be related to the C – O stretching in alcohol groups. Accordingly, all the samples show O – H stretching bands between 3230 and 3550 cm^{-1}. However, the change in peak positions for the samples evidence wide differences in the chemical environment of their hydroxyl groups. Samples of W-GQDs and CDs clearly show the alcohol bending vibrations, respectively at 1432 and 1402 cm^{-1}. More specifically, the peak of W-GQDs is compatible with aryl alcohols or phenols, while the peak in CDs is consistent with alkyl OHs. In contrast, the other two samples S-GQDs and E-GQDs show less prominent OH bending peaks, pointing to the prevalence of carbonyl-based groups in their structure. Surprisingly, the simultaneous rise of bands at 1224 and 872 cm^{-1} in the S-GQDs sample reveals the presence of oxirane rings in its structure [33], not being present in any of the other samples here reported. This observation would be related to the presence of a band shoulder at 3547 cm^{-1}, which is typically produced by the stretching vibration of internally bonded hydroxyl groups. Besides, bands at 1059 cm^{-1} to 1079 cm^{-1} would also point to the possible existence of alkyl ether groups in the S-GQD and E-GQD samples. In the CD sample, the 1076 cm^{-1} band is ascribable to the C-N stretching of primary amines. The IR spectrum of CDs reveals the presence of alcohols, carboxylic acids, and even amides (see Table 1), supporting that in this case, the main mechanism for the formation of nanoparticles is the condensation between the carboxylic groups of citric acid and the amines of ethylenediamine.

NMR characterization of CDs confirmed the condensation mechanism of formation (Figure 4). Proton (^1H) experiment showed that all the signals are found in the aliphatic region of the

spectrum, meaning that no conjugated structures are found in this sample, in contrast with their abundant presence in the GQDs samples. In particular, the overlapping triplets in the range of 4.1-3.2 ppm are related to the protons located on the ethylenediamine repetitive unit, while the thick group of signals between 3.2-2.3 ppm corresponds to the methylenes of the citric acid repetitive unit. The singlet at 3.3 ppm belongs to traces of ethylenediamine. Furthermore, carbon (^{13}C, APT: attached proton test) NMR experiment indicates that three types of carbon are present in CDs, namely the sp^2 carbon of amides and carboxylic acids (182-148 ppm), the quaternary carbon belonging to citric acid (75-71 ppm) and the methylenes belonging to citric acid and ethylenediamine (46-35 ppm). These findings suggest that the structure of the reagents is preserved along with the nanoparticle formation and that polycondensation is the main mechanism responsible for their growth [24].

Unfortunately, the NMR analysis of the GQDs was not informative, since the large content of quaternary carbon, the various and heterogeneous electronic environments in which the same structural feature can be found and the aggregation-dispersion equilibriums governing the stability of the nanoparticles in solution contributed altogether to the weakening and broadening of the NMR response of these materials.

The analysis by XPS provided information for the understanding of the surface chemistry and structural organization in the nanoparticles. First of all, XPS spectra allow an evaluation of the elemental composition (Table 2). Interestingly, depending on the method employed for the nanoparticle synthesis, the rate of oxidation, as elemental oxygen percentage, is distinct. The electrochemistry route is the mildest one, with a relatively low 18 at.% of oxygen. In contrast, the strong chemical oxidizing conditions for the preparation of W-GQDs and S-GQDs are reflected in the increase in the elemental oxygen to ca. 30%. In the case of CDs, the elemental analysis is consistent with the polyamide structure of these nanoparticles. The elemental oxygen amounts to 20%, and a high nitrogen content of 12% is achieved. The substantial amount of

nitrogen is differential in CDs, while it remains below the 2% level in the other three samples. Besides, the W-GQD and S-GQD samples show sulphur levels in the range of 4-6%, which can come from the sulfuric acid utilized for their preparation. However, no sulphur reactant is used for E-GQDs, so its 3.5% of sulphur probably accumulates from the graphite precursor.

The high resolution C 1s spectra for the nanoparticles (Figure 5) evidence substantial differences in their structure and oxygenated chemical groups. Typically, the C 1s region of carbon materials includes contributions from C – C bonds (single and double) and other carbon bonds with heteroatoms, in particular oxygen. Graphite and hexagonal sp^2 carbon domains generate intrinsically asymmetric peaks that should be modelled by asymmetric mathematical functions at a theoretical binding energy (BE) of 284.4 eV [34, 35]. The other carbon environments give nearly symmetric peak contributions that are usually well represented by Voigt-type functions with varying percentages of Gaussian and Lorentzian components and different BEs [36, 37]. Accordingly, the C 1s spectral profiles of the four carbon nanoparticles were analysed, and the results and assignments are presented in Figure 5 and Table 3.

Both the W-GQD and S-GQD samples contain a graphitic contribution at 284.4 eV, which nearly embodies the 20% of the total peak area. The presence of graphitic domains is in good agreement with TEM observations. The S-GQD sample keeps a small shake-up (π – π^*) contribution at 291.3 eV, which is consistent with a relatively low-defective graphitic structure. On the contrary, the π – π^* contribution seems to be lost in the W-GQD sample. The main C – O component of W-GQDs and S-GQDs is located at different BEs, respectively at 286.3 and 287.3 eV. This fact is in good agreement with IR observations, which showed oxirane and anhydride signals only in S-GQDs. Both W-GQD and S-GQD nanoparticles show a contribution at around 289 eV, with ca. 10% of the total area, which can be related to carboxylic acids [36], in agreement with IR spectra.

The interpretation of the C 1s spectrum for the E-GQD sample is not easy. At first sight, the profile looks like a classical graphite material, and it would be quite well fitted by an asymmetric line shape with a small shake-up contribution at 290.7 eV. However, it has been shown above that the oxidation rate in E-GQD nanoparticles barely reaches ca. 20 at.% of oxygen. As a consequence, most of the asymmetry in the C 1s spectrum should be assigned to C – O and carboxylic groups [38], in agreement with IR results, but not to an intrinsic graphitic characteristic. Following this idea, we assign the peak at BE = 285 eV both to tetrahedral sp^3 and to planar sp^2 carbon environments. The shake-up component at 290.7 eV would be associated to conjugated sp^2 carbon environments, but not to extended graphene domains [39]. This assignment is in agreement with TEM observations, which did not detect the presence of graphene layers in the core of E-GQD nanoparticles. The contributions at BEs of 286.0 and 288.1 eV can be assigned to C – O bonds from alcohol/ether groups and carboxylic acids, according to the IR interpretation. Therefore, the structure of E-GQD nanoparticles might be given by heterogeneous aromatic structures, whose extension is limited by the abundant presence of sp^3 and oxidized carbon.

In CD nanoparticles, the C 1s spectrum shows contributions of C – C/N – C bonds at 285.1 eV, C – O at 286.6 eV and amide and carboxylic groups at 288.4 eV. No C=C double bonds are present in CDs.

The XPS characterization is herein completed with some comments about O 1s and N 1s spectral regions (Tables 3 and 4). The O 1s and N 1s spectral profiles are quite simple and not shown for brevity. The O 1s band of W-GQDs and S-GQDs can be decomposed into two contributions at 532 and 533 eV, which have totally different percentages of the area in each sample. This fact confirms the presence of different functional groups on the W-GQD and S-GQD samples, in good agreement with the above comments on the C 1s region and IR assignments. The E-GQDs show a main component at 531.8 eV, mostly due to alcohol and

ether groups. The CD sample shows two components at 531.7 and 532.2 eV, which can be assigned to alcohol, amide and carboxylic acid groups. The four nanoparticle samples show relatively simple narrow O 1s contributions, but all of them are different from each other and thus characteristic of the material.

Regarding the N 1s region, a component due to structural nitrogen appears in all the samples at around 400 eV. Residual NO_2 is detected in S-GQDs at 401.8 eV. The most prominent signal was logically observed for CDs because of the high nitrogen content of approximately 12 at.%. The amide and amine joint contribution is found at 400.4 eV.

The morphological, structural and chemical characterization of W-GQDs, S-GQDs, E-GQDs and CDs reveals that features such as the presence or absence of conjugation and graphene domains, the rate of oxidation and the type of oxygenated groups strongly depend on the choice of the preparation method. Upon one route or another, one may attain entirely different materials with markedly distinct composition and features. Acid oxidation routes promoted by thermal (W-GQD) or sonochemical (S-GQD) approaches offer a compromise between the preservation of graphitic crystalline domains and the generation of oxygenated moieties. The formation of oxirane rings, ethers, cyclic anhydrides, alcohols and carboxylic acids can be favoured, the choice providing different strategies for further chemical modifications. The electrochemical oxidation (E-GQD) leads to a disordered structure of conjugated carbon bearing functional groups such as ether, alcohols and carboxylic acids. Finally, the bottom-up approach (CDs) supplies an easy route for the preparation of completely non-conjugated polymeric nanoparticles carrying abundant carboxylic acid and amine functionalities.

3.2. Optical properties

For the investigation of optical properties, absorption spectroscopy and steady-state fluorescence spectroscopy studies were performed (Figure 6). Because of an intense

contribution of heterogeneous conjugated π-domains, it is not possible to identify clear absorption bands in the UV region for S-GQDs and E-GQDs. In W-GQDs, three weak bands can be observed at 290, 330 and 365 nm. While a precise structural attribution of these bands is not straightforward, their energy positions suggest that they all originate from π-π^* transitions, belonging to aromatic structures with different oxygenated groups. The UV/Vis spectrum of CDs presents two defined absorption bands at 240 and 350 nm, related to n-π^* transitions of individual C=O and jointly interacting C=O, respectively. On the other hand, all the samples display fluorescence emission, with the maximum intensity respectively located at 440 nm for W-GQDs (λ_{exc} =340 nm), 550 nm for S-GQDs (λ_{exc} =440 nm), 450 nm for E-GQDs (λ_{exc}=360 nm) and 450 nm for CDs (λ_{exc}=370 nm). Quantum yields, calculated using quinine as standard, follow the trend: S-GQDs (<1%) < E-GQDs (1%) < W-GQDs (4.9%) < CDs (62%). Interestingly, while E-GQDs show an excitation dependent behaviour, for the other nanoparticles the emission does not depend on the excitation wavelength.

The observed optical behaviour can be scrutinized in view of the structural differences between the samples (Figure 7). E-GQDs present the lowest oxidation rate, as well as a number of heterogeneous conjugated structures. Therefore, sp^2 carbon structures of different sizes provide a distribution of energy states accessible with different excitation wavelengths (Figure 7a) [40]. Even if graphitic structures were found in W-GQDs and S-GQDs, the high amount of oxygenated functional groups decorating the domains acts as electron traps, supplying a preferential radiative pathway for the relaxation [41], independent of the excitation wavelength. Furthermore, the type of functional groups on the nanoparticles can tune the energy of the trap states (Figure 7b). In W-GQDs, carboxylic acids might act as electron acceptors, defining the energy of the excited state and producing the blue emission (λ_{em}=430 nm). In contrast, the green emission observed for S-GQDs (λ_{em}=550 nm) can be due to the destabilization of the HOMO, as it can be observed from the larger excitation wavelength, and the existence of electron traps

at lower energy, which is consistent with the presence of cyclic anhydrides delimiting the graphitic structures. Finally, the CD fluorescent behaviour is not linked to conjugated structures, which are absent in these nanoparticles. In previous studies, the mechanism behind the fluorescence emission of CDs has been related to the crosslink-enhanced emission effect. In particular, it was demonstrated that photo-induced charge transfer between amides and carboxylic acids takes place in the polymer structure [24]. Therefore, the emission energy does not depend on the excitation wavelength.

Gathering the information from the optical studies, the direct relationship between the structure (presence or absence of conjugation, quantity and type of functional groups) and the fluorescent behaviour is apparent. In this regard, only a few clear associations have been previously described in the literature. In particular, luminescence changes have been observed after the incorporation of a specific amino group on the nanoparticle, in agreement with theoretical calculations on its charge transfer effect [42]. Thus, it is here showed how the choice of the preparation method is determinant for preferentially addressing certain aspects of the fluorescence in carbon nanoparticles.

3.3. Biocompatibility to intestinal cells

Finally, the toxicity of carbon nanoparticles was studied on Caco-2 human intestinal cells, through the *in-vitro* assessment of cell viability using the MTT method. The effect of the nanoparticle samples was evaluated in human colon epithelium cells at two different stages of differentiation: undifferentiated cells (4 days after seeding) are considered cancer cells and differentiated cells (14 days after seeding) are considered normal cells. The samples were tested at various dilutions as it is shown in Figures 8 and 9. The IC_{50} (the concentration at which 50% of the cells died) of the different samples was calculated using data from concentration-response curves.

The W-GQD sample did not have effects on the viability of normal cells at any of the tested concentrations (0.0007-7 $ng \cdot \mu L^{-1}$) (Figure 8a). However, the concentrations of 0.7 and 7 $ng \cdot \mu L^{-1}$ decreased the viability of cancer cells with an IC_{50} of 0.15 $ng \cdot \mu L^{-1}$ (95% confidence interval log $IC_{50} = -0.79 \pm 0.21$). The effect of S-GQDs was qualitatively quite similar to W-GQDs, decreasing the viability of cancer cells with an IC_{50} of 4.62 $ng \cdot \mu L^{-1}$ (95% confidence interval log $IC_{50} = 0.62 \pm 1.12$). Also, CDs did not have effects on the viability of normal cells, while concentrations of 1 and 10 $ng \cdot \mu L^{-1}$ decreased the viability of cancer cells with an IC_{50} of 0.69 $ng \cdot \mu L^{-1}$ (95% confidence interval log $IC_{50} = -0.15 \pm 0.11$). A different behaviour was observed with the E-GQDs, which did not show any effect on the viability of both normal and cancer cells.

Two main factors seem to govern the biological effect of nanoparticles, namely, their size and oxygen functional groups. Besides, the toxicological outcome is logically dependent on the nanoparticle concentration [43] and cell line. It is generally accepted that GQDs are non-cytotoxic, presenting good biocompatibility both *in vitro* and *in vivo*, as demonstrated by many authors [44, 45]. Regarding size, GQDs are usually not big enough to pierce the cell membrane, which is a possible cause of cell killing, permeating well across the cell barriers [46]. Considering oxygen groups, it is known that GO may cause chemical toxicity by the generation of reactive oxygen species (ROS) [47, 48]. On the contrary, GQDs do not typically exhibit toxicity in indirect enzymatic tests, at least at short incubation times and certain cell lines, even though GQDs possess large amounts of functional groups [44].

Despite the overall biocompatibility of GQDs, certain studies have proven differential biocide properties under particular cell environments. For instance, Biswas et al. [45] reported >90% cell viability for GQDs on fibroblast and kidney cell lines in a wide range of concentrations (up to 200 $\mu g \cdot mL^{-1}$), together with antibacterial activity against *E. coli*; the ROS generation played a key role in the behaviour. Results like this show that GQDs can behave as a selective killer

of specific cells, while remaining innocuous to the rest, even without any anchored drug, targeting moieties or toxicity mitigating agents. In our case, three samples, namely W-GQDs, S-GQDs and CDs, do not have negative effects on the viability of normal cells in a wide range of concentrations, while they act on the cancer cells at specific concentrations. This behaviour has been rarely observed for pristine carbon nanoparticles [49, 50]. Therefore, these nanoparticles might be applied in therapeutics against cancer cells. The E-GQD sample is innocuous for both normal and cancer cells, so it might have an application as a vehicle for pharmaceuticals in drug delivery.

The different behaviour of E-GQDs provides an additional hint about the anticancer activity of W-GQDs, S-GQDs and CDs. Given that changes in particle size (W-GQDs ≈ S-GQDs > E-GQDs ≈ CDs) cannot logically explain the difference, its origin has to be sought at the surface chemistry level. According to the XPS analysis, E-GQDs present the lowest oxygen quantity (Table 2), as well as the most uniform distribution of functional groups (Table 4). The other types of carbon nanoparticles (W-GQDs, S-GQDs and CDs) bear a wide variety of oxygen groups, including those with high oxygen-to-carbon ratios (anhydride, carboxylic acid, etc.). The presence of highly oxygenated functional groups might lead to the differential response from cancer cells, probably through the generation of ROS.

Conclusions

In this study, the preparation of GQDs was achieved by means of three different top-down approaches, all involving the oxidative cutting of graphite or GO carbon materials. Here, the employment of a strong chemical oxidizer and high temperature, sonication or electrochemical oxidation conferred respectively to W-GQDs, S-GQDs and E-GQDs unique chemical and optical properties. In addition, the bottom-up synthesis of CDs provided a fourth type of fluorescent nanostructure for comparison. Interestingly, the structural characterization of the

GQD samples showed how critical factors such as extension of the conjugated π-domains, rate of oxidation and type of oxygenated moieties can be controlled through the choice of the appropriate preparation method. The size of graphene domains decreases in the order of W-GQD > S-GQD > E-GQD. Actually, the aromatic domains in the E-GQDs are much limited by a number of tetrahedral sp^3 defects. Furthermore, microwave irradiation of ethylenediamine and citric acid resulted in polymeric non-conjugated CDs rich of functional groups, offering a completely distinct type of nanoparticles.

The absorption and fluorescence spectroscopy studies highlighted the direct relationship between the reported structures and the optical properties of the synthetized materials. In here, the dependence of the fluorescence emission from excitation was affected by the rate of oxidation, since oxygen moieties can act as electron traps that emit independently from the excitation wavelength. Moreover, the type of oxygen groups showed an influence on the emission energy. While GQDs with only carboxylic acids emitted in the blue, GQDs carrying cyclic anhydrides showed green fluorescence. Finally, CDs fluorescence was not related to the presence of conjugated structures, which are absent in these nanoparticles, but rather attributed to the crosslink-enhanced emission effect.

Lastly, the cytotoxicity of the nanoparticles was tested *in vitro* on intestinal human cells, proving that all carbon nanoparticles are biocompatible towards a normal human cell line, while in turn some of them exhibit a clear concentration-dependent anticancer activity against the equivalent cancer cells. This opens up exciting prospects for the use of these nanoparticles in colon cancer theranostics. Overall, we have shed light into the vast and complex pool of knowledge regarding the synthesis and applications of fluorescent carbon nanoparticles. In summary, the preparation method is a critical issue that should be paid attention to, since it completely rules the morphology, chemical composition, photoluminescence and biological behavior of nanoparticles thereof.

Acknowledgements

This work has been funded by MINEICO under project ENE2016-79282-C5-1-R, the Gobierno de Aragón (Grupo Reconocido T03-17R + E19-17R + A02-17R) and respective associated EU Regional Development Funds. J.M.G.-D. greatly acknowledges Spanish Ministry of Science, Innovation and Universities (MICINN, formerly MINEICO) for his "Juan de la Cierva – incorporación" grant (Ref. UCI-2016-27789). Special thanks are directed to Ms. L. Martinez for helping with the W-GQD preparation, the Analysis Service at Instituto de Carboquímica ICB-CSIC and the Electron Microscopy Service at the University of Zaragoza. ICN2 is supported by the Severo Ochoa program from Spanish MINECO (Grant No. SEV-2017-0706).

References

[1] X. Xu, R. Ray, Y. Gu, H.J. Ploehn, L. Gearheart, K. Raker, W.A. Scrivens, Electrophoretic analysis and purification of fluorescent single-walled carbon nanotube fragments, Journal of the American Chemical Society 126(40) (2004) 12736-12737.
[2] X. Zheng, A. Ananthanarayanan, K. Luo, P. Chen, Glowing graphene quantum dots and carbon dots: properties, syntheses, and biological applications, Small 11(14) (2015) 1620-1636.
[3] R. Guo, S. Zhou, Y. Li, X. Li, L. Fan, N. Voelcker, Rhodamine-functionalized graphene quantum dots for detection of Fe^{3+} in cancer stem cells, ACS Applied Materials & Interfaces 7(43) (2015) 23958-23966.
[4] S. Li, S. Zhou, Y. Li, X. Li, J. Zhu, L. Fan, S. Yang, Exceptionally high payload of the IR780 iodide on folic acid-functionalized graphene quantum dots for targeted photothermal therapy, ACS Applied Materials & Interfaces 9(27) (2017) 22332-22341.
[5] Y. Liu, S. Zhou, L. Fan, H. Fan, Synthesis of red fluorescent graphene quantum dot-europium complex composites as a viable bioimaging platform, Microchimica Acta 183(9) (2016) 2605-2613.
[6] X. Tan, Y. Li, X. Li, S. Zhou, L. Fan, S. Yang, Electrochemical synthesis of small-sized red fluorescent graphene quantum dots as a bioimaging platform, Chemical Communications 51(13) (2015) 2544-2546.
[7] M. Zhang, L. Bai, W. Shang, W. Xie, H. Ma, Y. Fu, D. Fang, H. Sun, L. Fan, M. Han, C. Liu, S. Yang, Facile synthesis of water-soluble, highly fluorescent graphene quantum dots as a robust biological label for stem cells, Journal of Materials Chemistry 22(15) (2012) 7461-7467.
[8] Y. Yan, J. Gong, J. Chen, Z. Zeng, W. Huang, K. Pu, J. Liu, P. Chen, Recent advances on graphene quantum dots: from chemistry and physics to applications, Advanced Materials 31(21) (2019) 1808283.
[9] Z. Luo, G. Qi, K. Chen, M. Zou, L. Yuwen, X. Zhang, W. Huang, L. Wang, Microwave-assisted preparation of white fluorescent graphene quantum dots as a novel phosphor for

enhanced white-light-emitting diodes, Advanced Functional Materials 26(16) (2016) 2739-2744.
[10] S. Chen, J.-W. Liu, M.-L. Chen, X.-W. Chen, J.-H. Wang, Unusual emission transformation of graphene quantum dots induced by self-assembled aggregation, Chemical Communications 48(61) (2012) 7637-7639.
[11] R. Ye, C. Xiang, J. Lin, Z. Peng, K. Huang, Z. Yan, N.P. Cook, E.L.G. Samuel, C.-C. Hwang, G. Ruan, G. Ceriotti, A.-R.O. Raji, A.A. Martí, J.M. Tour, Coal as an abundant source of graphene quantum dots, Nature Communications 4 (2013) 2943.
[12] D. Iannazzo, A. Pistone, S. Ferro, L. De Luca, A.M. Monforte, R. Romeo, M.R. Buemi, C. Pannecouque, Graphene quantum dots based systems as HIV inhibitors, Bioconjugate Chemistry 29(9) (2018) 3084-3093.
[13] P. Tian, L. Tang, K.S. Teng, S.P. Lau, Graphene quantum dots from chemistry to applications, Materials Today Chemistry 10 (2018) 221-258.
[14] J. Peng, W. Gao, B. Gupta, Z. Liu, R. Romero-Aburto, L. Ge, L. Song, L. Alemany, X. Zhan, G. Gao, S. Vithayathil, B. Kaipparettu, A. Marti, T. Hayashi, J. Zhu, P. Ajayan, Graphene quantum dots derived from carbon fibers, Nano Letters 12(2) (2012) 844-849.
[15] J. Lu, J. Yang, J. Wang, A. Lim, S. Wang, K. Loh, One-Pot Synthesis of fluorescent carbon nanoribbons, nanoparticles, and graphene by the exfoliation of graphite in ionic liquids, ACS Nano 3(8) (2009) 2367-2375.
[16] S. Yang, S. Bruller, Z. Wu, Z. Liu, K. Parvez, R. Dong, F. Richard, P. Samori, X. Feng, K. Mullen, Organic radical-assisted electrochemical exfoliation for the scalable production of high-quality graphene, Journal of the American Chemical Society 137(43) (2015) 13927-13932.
[17] X. Hai, J. Feng, X. Chen, J. Wang, Tuning the optical properties of graphene quantum dots for biosensing and bioimaging, Journal of Materials Chemistry B 6(20) (2018) 3219-3234.
[18] H. Jiang, J. Li, J. Jiang, Y. Wang, X. Nie, X. Zhang, B. Liu, J. Zhang, Systematic assessment of the toxicity and potential mechanism of graphene derivatives in vitro and in vivo, Toxicological Sciences 167(1) (2018) 269-281.
[19] D. Iannazzo, I. Ziccarelli, A. Pistone, Graphene quantum dots: multifunctional nanoplatforms for anticancer therapy, Journal of Materials Chemistry B 5(32) (2017) 6471-6489.
[20] D.H. Kim, T.W. Kim, Ultrahigh current efficiency of light-emitting devices based on octadecylamine-graphene quantum dots, Nano Energy 32 (2017) 441-447.
[21] M. Dinari, M.M. Momeni, M. Goudarzirad, Dye-sensitized solar cells based on nanocomposite of polyaniline/graphene quantum dots, Journal of Materials Science 51(6) (2016) 2964-2971.
[22] T. Feng, S. Zhu, Q. Zeng, S. Lu, S. Tao, J. Liu, B. Yang, Supramolecular cross-link-regulated emission and related applications in polymer carbon dots, ACS Applied Materials & Interfaces 10(15) (2018) 12262-12277.
[23] L. Xiao, H. Sun, Novel properties and applications of carbon nanodots, Nanoscale Horizons 3(6) (2018) 565-597.
[24] L. Vallan, E. Urriolabeitia, F. Ruiperez, J. Matxain, R. Canton-Vitoria, N. Tagmatarchis, A. Benito, W. Maser, Supramolecular-enhanced charge transfer within entangled polyamide chains as the origin of the universal blue fluorescence of polymer carbon dots, Journal of the American Chemical Society 140(40) (2018) 12862-12869.
[25] J.A. Jaleel, K. Pramod, Artful and multifaceted applications of carbon dot in biomedicine, Journal of Controlled Release 269 (2018) 302-321.
[26] J. Li, B. Tang, B. Yuan, L. Sun, X. Wang, A review of optical imaging and therapy using nanosized graphene and graphene oxide, Biomaterials 34(37) (2013) 9519-9534.

[27] J. Ge, M. Lan, B. Zhou, W. Liu, L. Guo, H. Wang, Q. Jia, G. Niu, X. Huang, H. Zhou, X. Meng, P. Wang, C. Lee, W. Zhang, X. Han, A graphene quantum dot photodynamic therapy agent with high singlet oxygen generation, Nature Communications 5 (2014) 4596.
[28] H. Li, X. He, Z. Kang, H. Huang, Y. Liu, J. Liu, S. Lian, C.H.A. Tsang, X. Yang, S.-T. Lee, Water-soluble fluorescent carbon quantum dots and photocatalyst design, Angewandte Chemie International Edition 49(26) (2010) 4430-4434.
[29] D.B. Shinde, V.K. Pillai, Electrochemical preparation of luminescent graphene quantum dots from multiwalled carbon nanotubes, Chemistry – A European Journal 18(39) (2012) 12522-12528.
[30] A. Ananthanarayanan, X. Wang, P. Routh, B. Sana, S. Lim, D.-H. Kim, K.-H. Lim, J. Li, P. Chen, Facile Synthesis of graphene quantum dots from 3d graphene and their application for Fe^{3+} sensing, Advanced Functional Materials 24(20) (2014) 3021-3026.
[31] J. Mesonero, L. Mahraoui, M. Matosin, A. Rodolosse, M. Rousset, E. Brotlaroche, Expression of the hexose transporters glut1-glut5 and sglt1 in clones of Caco-2 cells, Biochemical Society Transactions 22(3) (1994) 681-684.
[32] F. Zucco, A. Batto, G. Bises, J. Chambaz, A. Chiusolo, R. Consalvo, H. Cross, G. Dal Negro, I. de Angelis, G. Fabre, F. Guillou, S. Hoffman, L. Laplanche, E. Morel, M. Pincon-Raymond, P. Prieto, L. Turco, G. Ranaldi, M. Rousset, Y. Sambuy, M. Scarino, F. Torreilles, A. Stammati, An inter-laboratory study to evaluate the effects of medium composition on the differentiation and barrier function of Caco-2 cell lines, Atla-Alternatives To Laboratory Animals 33(6) (2005) 603-618.
[33] J. Coates, Interpretation of Infrared spectra, a practical approach, in: R.A. Meyers (Ed.), Encyclopedia of Analytical Chemistry, Wiley, Chichester, 2000, pp. 10815-10837.
[34] F. Sette, G.K. Wertheim, Y. Ma, G. Meigs, S. Modesti, C.T. Chen, Lifetime and screening of the C 1s photoemission in graphite, Physical Review B 41(14) (1990) 9766-9770.
[35] R. Blume, D. Rosenthal, J.-P. Tessonnier, H. Li, A. Knop-Gericke, R. Schlögl, Characterizing graphitic carbon with X-ray photoelectron spectroscopy: a step-by-step approach, ChemCatChem 7(18) (2015) 2871-2881.
[36] J.L. Figueiredo, M.F.R. Pereira, The role of surface chemistry in catalysis with carbons, Catalysis Today 150(1) (2010) 2-7.
[37] G. Levi, O. Senneca, M. Causà, P. Salatino, P. Lacovig, S. Lizzit, Probing the chemical nature of surface oxides during coal char oxidation by high-resolution XPS, Carbon 90 (2015) 181-196.
[38] Y. Li, Y. Hu, Y. Zhao, G. Shi, L. Deng, Y. Hou, L. Qu, An electrochemical avenue to green-luminescent graphene quantum dots as potential electron-acceptors for photovoltaics, Advanced Materials 23(6) (2011) 776-780.
[39] J. Matthew, Surface analysis by Auger and x-ray photoelectron spectroscopy. D. Briggs and J. T. Grant (eds). IMPublications, Chichester, UK and SurfaceSpectra, Manchester, UK, 2003. 900 pp., ISBN 1-901019-04-7, 900 pp, Surface and Interface Analysis 36(13) (2004) 1647-1647.
[40] M.-H. Jang, S.H. Song, H.D. Ha, T.S. Seo, S. Jeon, Y.-H. Cho, Origin of extraordinary luminescence shift in graphene quantum dots with varying excitation energy: An experimental evidence of localized sp^2 carbon subdomain, Carbon 118 (2017) 524-530.
[41] S. Wang, I.S. Cole, D. Zhao, Q. Li, The dual roles of functional groups in the photoluminescence of graphene quantum dots, Nanoscale 8(14) (2016) 7449-7458.
[42] S. Jin, D. Kim, G. Jun, S. Hong, S. Jeon, Tuning the photoluminescence of graphene quantum dots through the charge transfer effect of functional groups, ACS Nano 7(2) (2013) 1239-1245.

[43] L. Liang, Z. Kong, Z. Kang, H. Wang, L. Zhang, J.-W. Shen, Theoretical evaluation on potential cytotoxicity of graphene quantum dots, ACS Biomaterials Science & Engineering 2(11) (2016) 1983-1991.
[44] Y. Chong, Y. Ma, H. Shen, X. Tu, X. Zhou, J. Xu, J. Dai, S. Fan, Z. Zhang, The in vitro and in vivo toxicity of graphene quantum dots, Biomaterials 35(19) (2014) 5041-5048.
[45] A. Biswas, P. Khandelwal, R. Das, G. Salunke, A. Alam, S. Ghorai, S. Chattopadhyay, P. Poddar, Oxidant mediated one-step complete conversion of multi-walled carbon nanotubes to graphene quantum dots and their bioactivity against mammalian and bacterial cells, Journal of Materials Chemistry B 5(4) (2017) 785-796.
[46] X. Wang, R. Lei, H. Huang, N. Wang, L. Yuan, R. Xiao, L. Bai, X. Li, L. Li, X. Yang, The permeability and transport mechanism of graphene quantum dots (GQDs) across the biological barrier, Nanoscale 7(5) (2015) 2034-2041.
[47] J. Frontinan-Rubio, M. Gomez, C. Martin, J. Gonzalez-Dominguez, M. Duran-Prado, E. Vazquez, Differential effects of graphene materials on the metabolism and function of human skin cells, Nanoscale 10(24) (2018) 11604-11615.
[48] M. Pelin, L. Fusco, C. Martin, S. Sosa, J. Frontinan-Rubio, J. Gonzalez-Dominguez, M. Duran-Prado, E. Vazquez, M. Prato, A. Tubaro, Graphene and graphene oxide induce ROS production in human HaCaT skin keratinocytes: the role of xanthine oxidase and NADH dehydrogenase, Nanoscale 10(25) (2018) 11820-11830.
[49] M. Pirsaheb, S. Mohammadi, A. Salimi, M. Payandeh, Functionalized fluorescent carbon nanostructures for targeted imaging of cancer cells: a review, Microchimica Acta 186(4) (2019).
[50] I.S. Raja, S.-J. Song, M.S. Kang, Y.B. Lee, B. Kim, S.W. Hong, S.J. Jeong, J.-C. Lee, D.-W. Han, Toxicity of zero- and one-dimensional carbon nanomaterials, Nanomaterials 9 (2019) 1214.

Table 1. IR frequencies of the prominent spectral bands and their assignments.

	IR frequency, wavenumber [cm^{-1}]			
Assignment	W-GQDs	S-GQDs	E-GQDs	CDs
Carbon backbone				
Vinyl (δ)	-	-	943	-
C = C (ν)	1610	1626	1643	-
Methylene (ν)	-	-	2860/2932	2928/3079
Oxygen functional groups				
Oxirane ring	-	872 + 1224	-	-
Alkyl ether (ν)	-	1059	1079	-
Alcohol C – O (ν)	1122	1146	1158	1186/1234
Alcohol O – H (δ)	1432	-	1400	1298/1340/1402/1437
Carboxylic acid	1726	1738	1714/1764	1709/1780
Cyclic acid anhydride	-	1815	-	-
Alcohol O – H (ν)	3234/3413	3409/3547	3246/3426	3246/3409
Nitrogen functional groups				
Amide C – N (ν)	-	-	-	1076/1186
Amide N – H (δ)	-	-	-	1563
Amide C = O (ν)	-	-	-	1653

Table 2. Quantitative analysis of the main elements by XPS, indicating the band regions that were used for quantification.

	Elemental content [at.%]				
	C (1s)	O (1s)	N (1s)	S (2p)	Other (2p)
W-GQDs	64.4	28.6	0.9	4.7	1.38 (Mn)
S-GQDs	62.0	30.5	1.3	6.2	-
E-GQDs	75.9	18.2	1.8	3.5	0.61 (P)
CDs	66.6	21.3	12.1	-	-

Table 3. Interpretation of high resolution C 1s spectra.

BE [eV]	% area	Assignment
W-GQDs		
284.5	19.2	Conjugated sp^2
285.1	49.6	sp^3
286.3	23.4	C – O
288.9	7.8	COOH
S-GQDs		
284.4	17.0	Conjugated sp^2
285.2	38.0	sp^3
287.3	33.8	C – O
289.2	10.1	COOH
291.3	1.2	Shake-up (π-π^*)
E-GQDs		
285.1	64.0	sp^2 + sp^3
286.0	24.1	C – O
288.1	6.7	COOH
290.7	5.3	Shake-up
CDs		
285.1	45.3	sp^3 + C – N
286.6	25.8	C – O
288.4	28.9	C = O

Table 4. Interpretation of high resolution O 1s spectra.

BE [eV]	% area	Assignment
W-GQDs		
531.9	60.5	alcohol, phenol
532.9	39.5	carboxylic acid
S-GQDs		
532.0	26.0	alcohol, phenol
		ether, cyclic anhydride, carboxylic
533.0	74.0	acid
E-GQDs		
531.8	100	alcohol, phenol
CDs		
531.7	57.9	alcohol
532.2	42.1	amide, carboxylic acid

Table 5. Interpretation of high resolution N 1s spectra.

BE [eV]	% area	Assignment
W-GQDs		
399.7	100	Structural
S-GQDs		
400.1	25.9	Structural
401.8	74.1	Residual NO_2
E-GQDs		
399.8	100	Structural
CDs		
400.4	100	Amide, amine

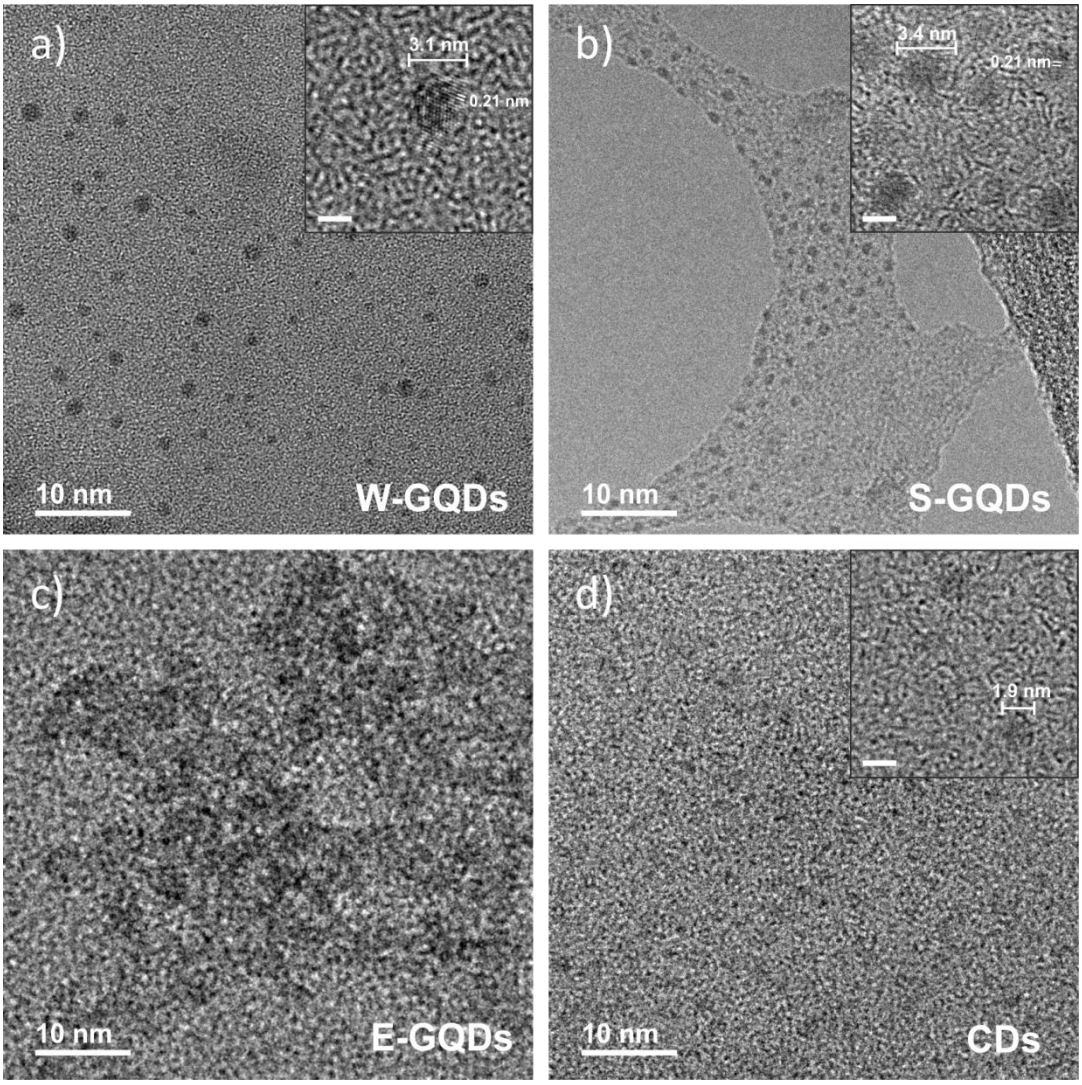

Figure 1. HRTEM images of (a) W-GQDs, (b) S-GQDs, (c) E-GQDs and (d) CDs. Insets: zoom up showing individual nanoparticles (scale bar: 2nm).

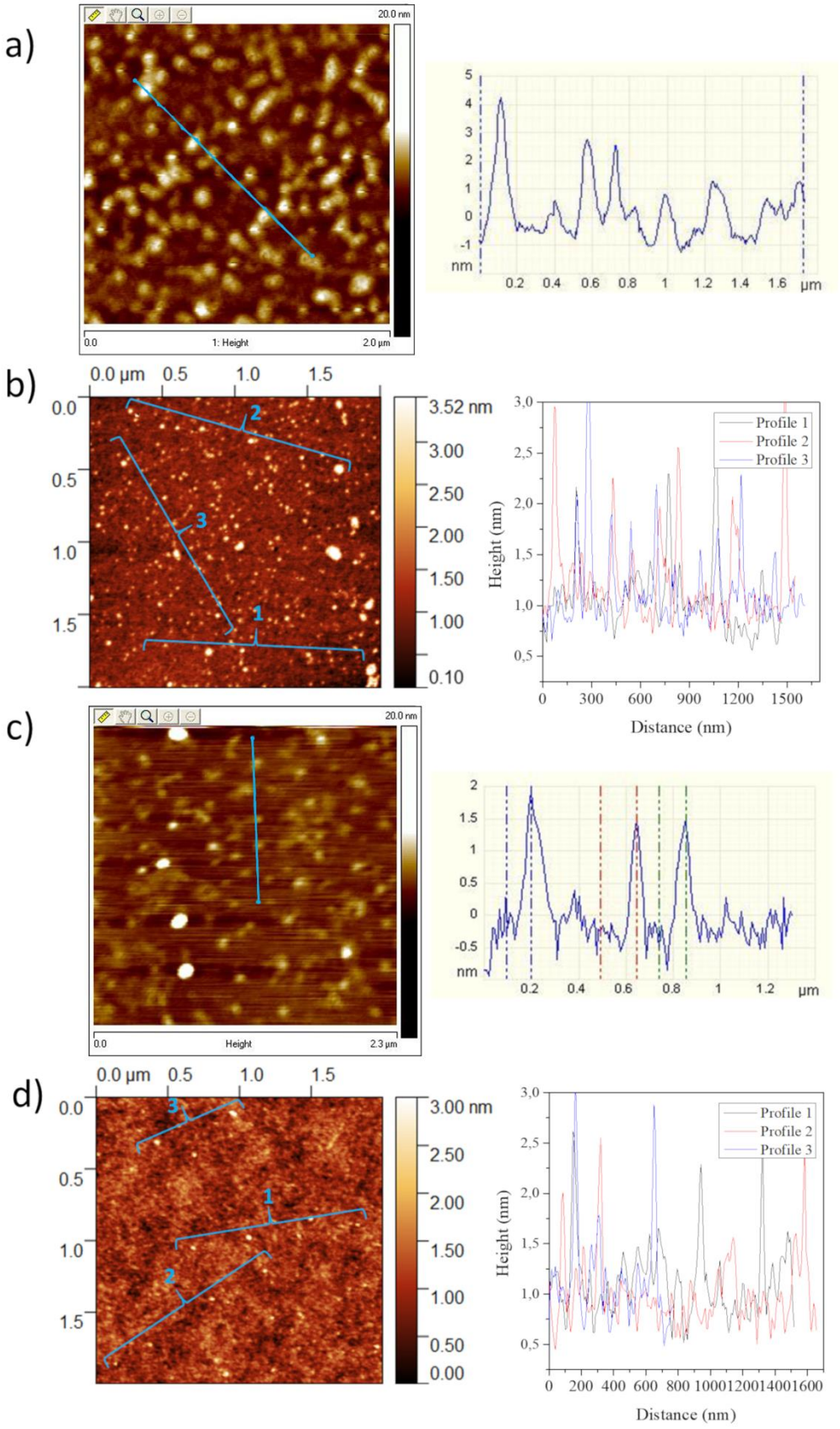

Figure 2. AFM images and height profiles of (a) W-GQDs, (b) S-GQDs, (c) E-GQDs and (d) CDs.

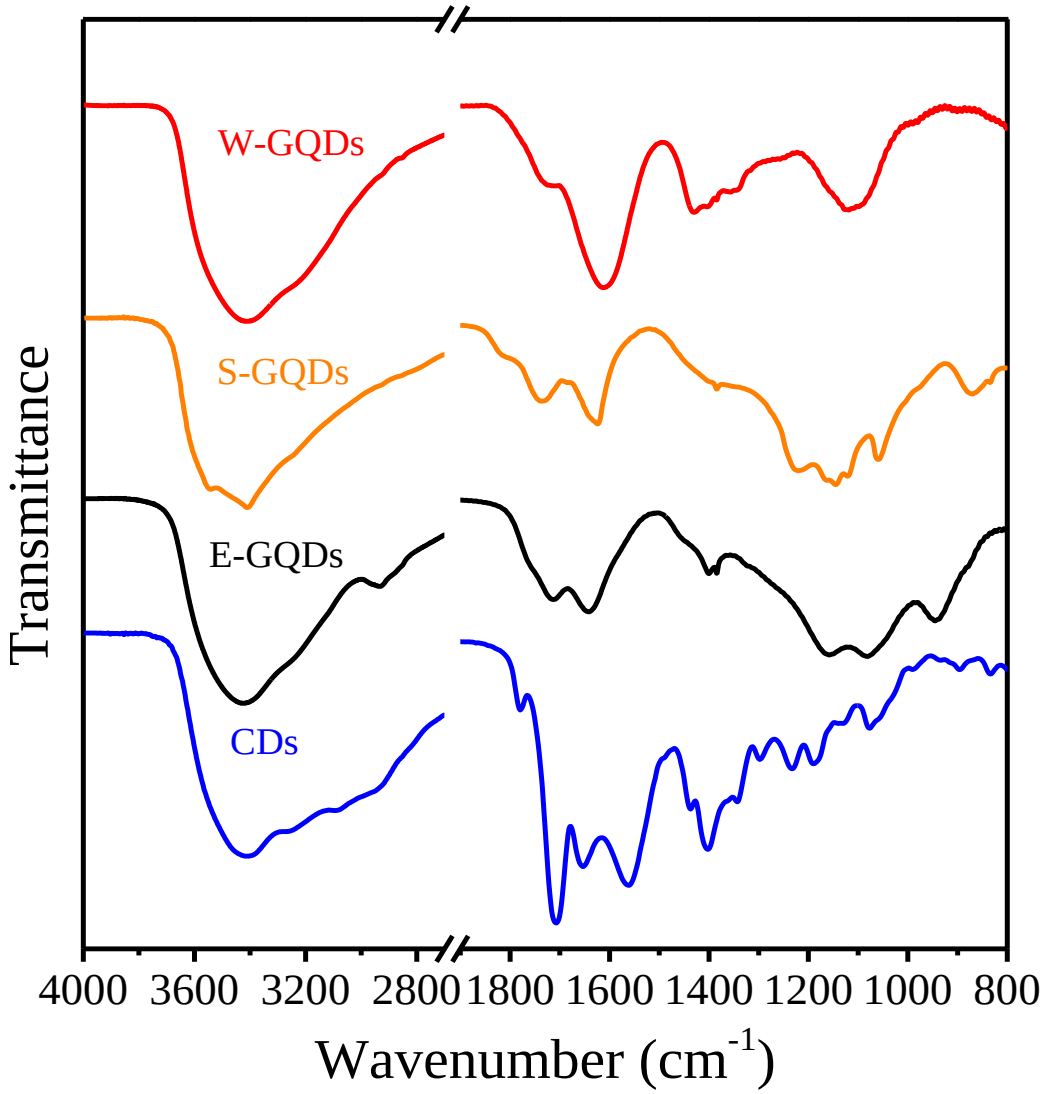

Figure 3. IR spectra of W-GQDs, S-GQDs, E-GQDs and CDs.

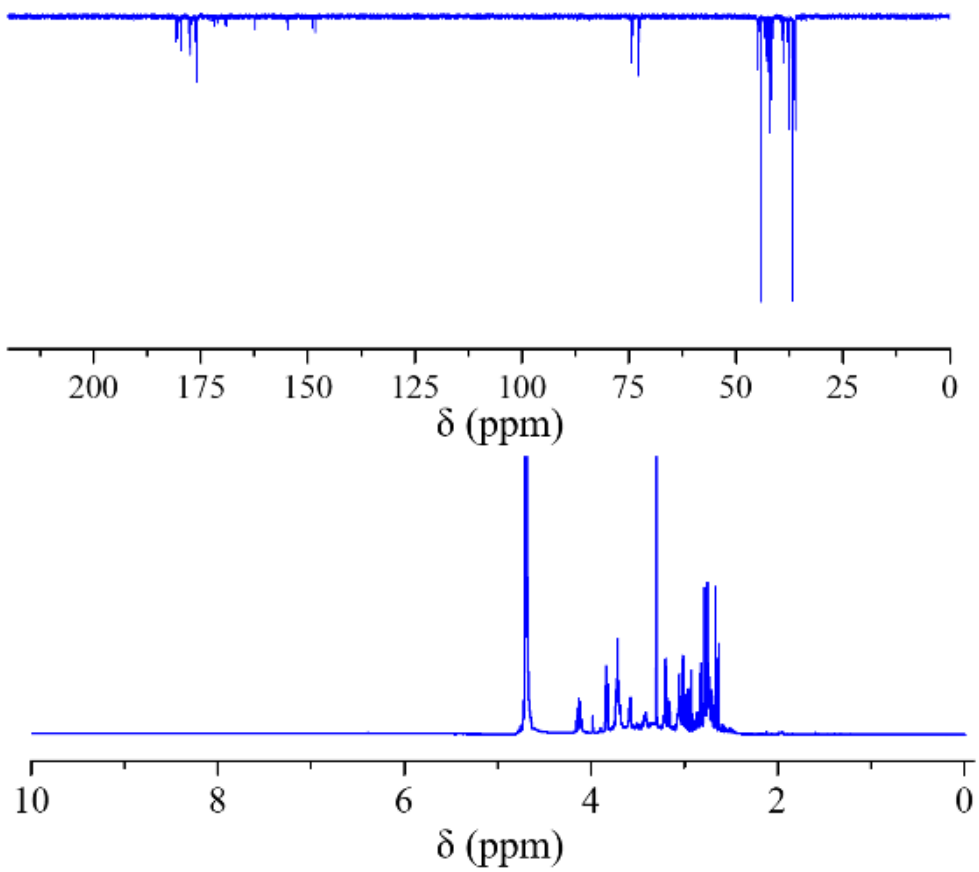

Figure 4. NMR spectra of CDs: ^{13}C APT (top) and ^{1}H NMR (bottom).

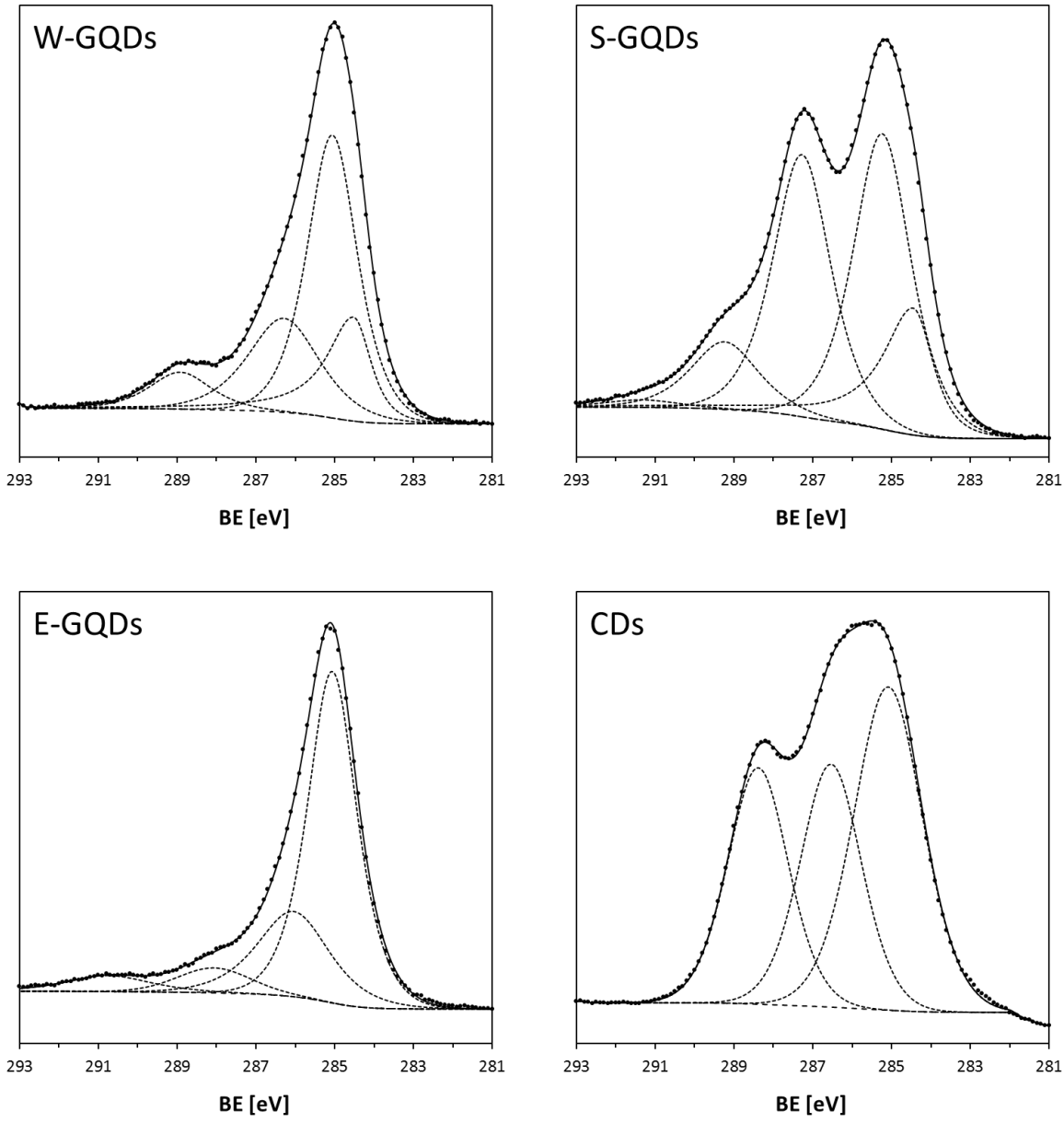

Figure 5. High resolution C 1s XPS spectra of W-GQDs, S-GQDs, E-GQDs and CDs.

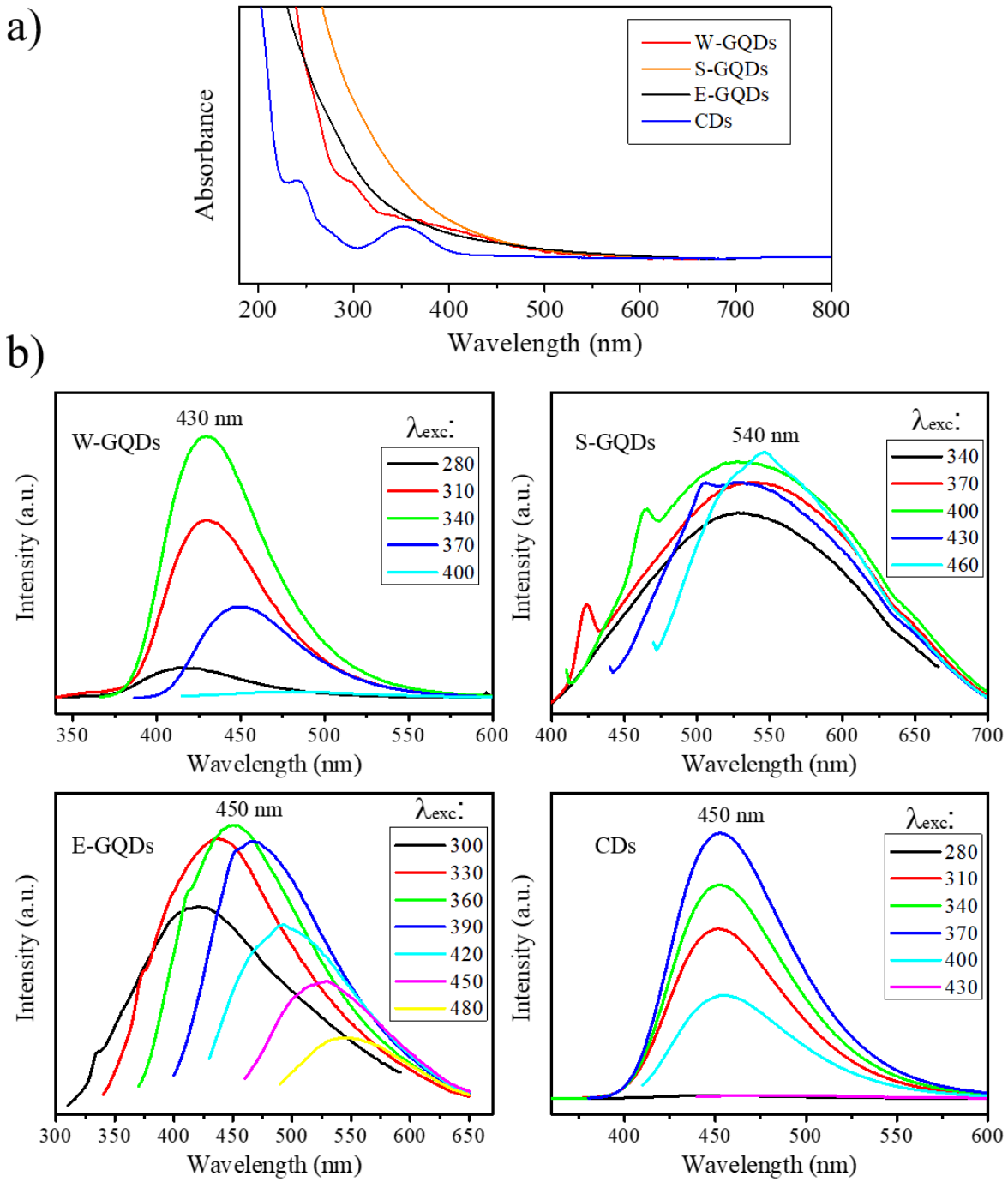

Figure 6. (a) absorption and (b) fluorescence emission at different excitation wavelength of W-GQDs, S-GQDs, E-GQDs and CDs.

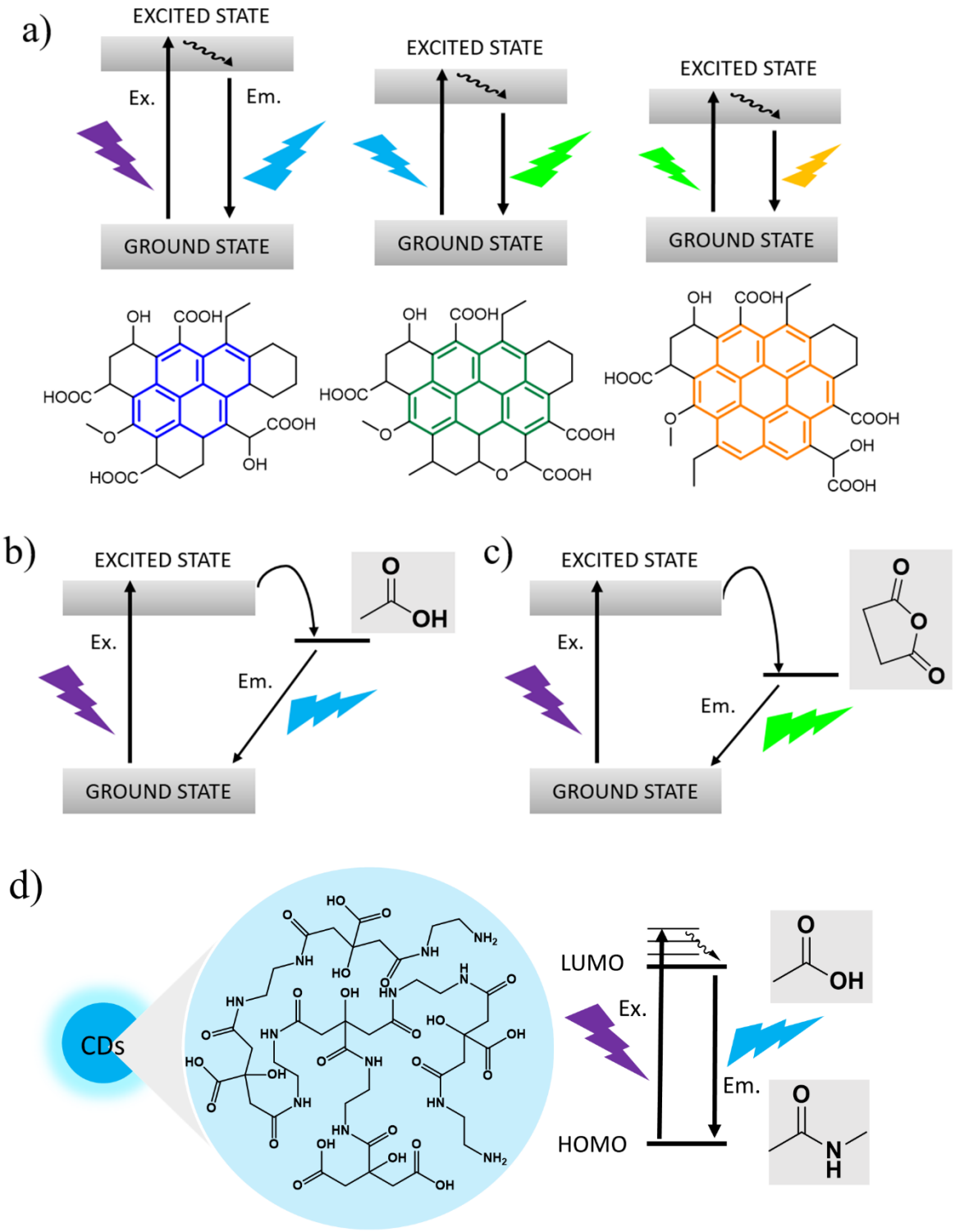

Figure 7. Diagram of fluorescence mechanisms in GQDs and CDs: a) heterogeneous conjugated structures are excited and emit at different wavelength, producing the excitation-dependent fluorescent behaviour of E-GQDs. b) carboxylic acids in W-GQDs and (c) cyclic anhydrides in S-GQDs can act as localized electron traps, (d) charge transfer between localized orbitals in CDs. The resulting emission in (b), (c) and (d) is independent from the excitation.

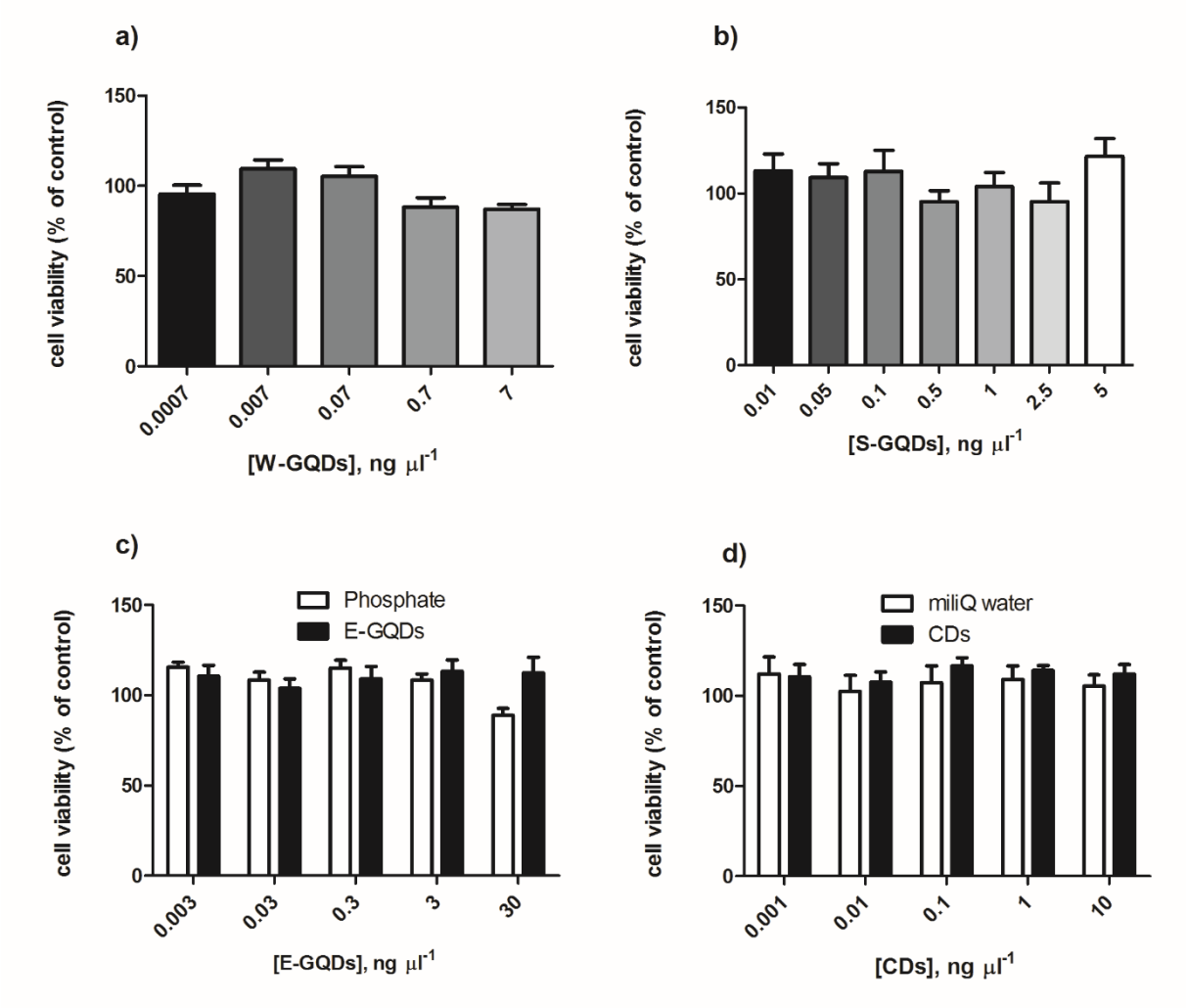

Figure 8. *In vitro* toxicity of W-GQDs (a), S-GQDs (b), E-GQDs (c) and CDs (d) on normal human intestinal cells (14 days after seeding). The results are expressed as mean ± SEM ($n \geq 12$ experiments).

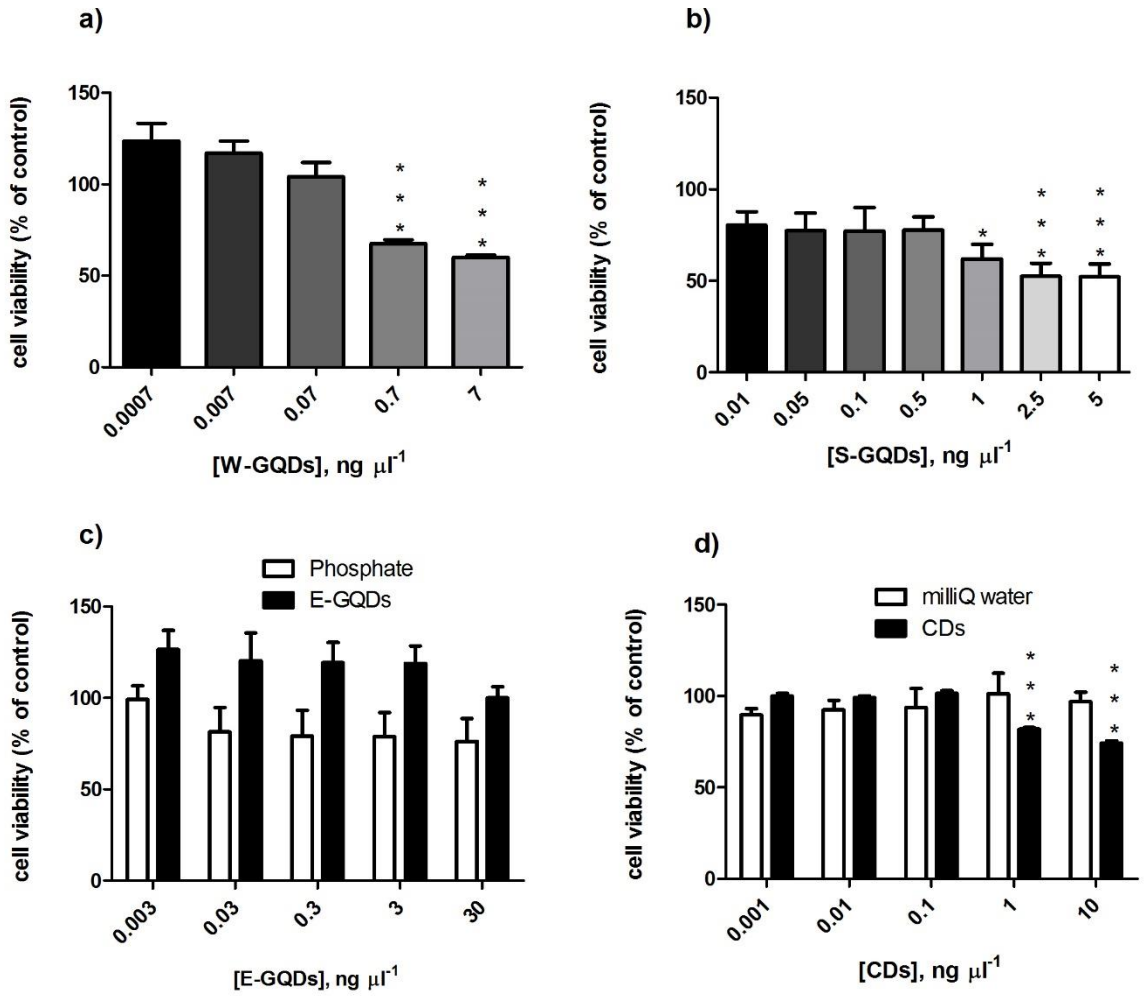

Figure 9. *In vitro* toxicity of W-GQDs (a), S-GQDs (b), E-GQDs (c) and CDs (d) on cancer human intestinal cells (4 days after seeding). The results are expressed as mean ± SEM (n ≥ 12 experiments) *P<0.05; ***P<0.001 vs. control.